

# Dimensional Accuracy of Thermoset Composites: Shape Optimization

QI ZHU AND PHILIPPE H. GEUBELLE\*

*Department of Aeronautical and Astronautical Engineering  
University of Illinois at Urbana-Champaign  
104 South Wright St., 306 Talbot Laboratory  
Urbana, IL 61801-2935, USA*

(Received June 15, 2000)  
(Revised November 21, 2000)

**ABSTRACT:** We present a design sensitivity analysis, which supports the shape optimization of the tool used in thermoset composite manufacturing. The method provides a systematic way to predict the optimal tool geometry that leads to the minimum difference between desired and final shapes of the manufactured part. The design process is formalized by integrating process modeling, design sensitivity analysis, and numerical optimization into a single framework. The process modeling is based on a transient coupled thermo-chemo-viscoelastic finite element scheme, which accurately captures the evolution of residual stresses throughout the manufacturing process, and their effect on the final shape of the composite part. Design sensitivity information is extracted efficiently from the primal analysis using an analytical, direct differentiation method. The sensitivities are then provided to a numerical optimization program to improve the tool design. Optimization results are presented for two specific applications involving mold design for cross-ply laminates and L-shaped composite parts.

**KEY WORDS:** thermoset composites, dimensional accuracy, design sensitivity analysis, shape optimization, finite elements.

## 1. INTRODUCTION

**A**UTOCLAVE CURING AND hot pressing are two manufacturing processes commonly used to fabricate high performance thermoset composites. During the processing, residual stresses build up in laminates owing to the mismatch of thermal expansion along and across the fibers as well as the cure shrinkage of the thermoset resin. These residual stresses lead to undesirable shape distortions when the cured components are released from the mold, and such distortions are often large enough to render the part unserviceable [1]. Process-induced warpage affects many facets of the composite industry. In the automotive industry, for example, warpage leads to problems with the fit and finish

---

\*Author to whom correspondence should be addressed.

of body panel components. Dimensional accuracy is critical when joining two body panels. High surface tolerances are also crucial in order to produce panels with smooth, glossy finishes. Engineers using conventional technology can spend significant time and resources in an expensive trial-and-error effort to eliminate warpage.

While considerable research effort has been devoted to the understanding and modeling of warpage in composite materials (see [2] for a brief literature review), little has been done using optimization techniques to achieve dimensional accuracy of manufactured composite parts. One approach for reducing warpage in polymer composite manufacturing is to optimize the cure cycle to reduce the residual stresses. In his early study, Weitsman [3] presented an analytical scheme for the optimal cooldown path for thin viscoelastic plates. His approach took into account the viscoelastic behavior of the polymeric matrix and consequently its stress relaxation capabilities. White and Hahn [4] experimentally investigated the control and reduction of processing-induced residual stresses for a graphite-BMI composite material by modifying processing conditions. The effects of dwell temperature, dwell time, cool-down rate, cool-down pressure, and postcure on residual stresses were examined using unsymmetric cross-ply laminates. Their results show that residual stresses can be reduced by as much as 25–30%. Olivier and Cottu [5] recently established an optimization approach for reducing residual stresses in thin laminates on the basis of a cure-kinetics and a thermomechanical model. They presented the simulation results as a three-dimensional diagram which allowed the determination of optimum cure temperature to minimize residual stresses.

However, even using the aforementioned approaches, it is often impossible to completely eliminate the residual stresses in the manufacturing of thermoset composites. When the requirement of dimensional accuracy is high, residual stresses may easily yield components out of tolerance and the components must be scrapped. Throughout much of the composite manufacturing industry the solution to component warpage is iteration of tool geometry until the final distorted component matches the desired shape. In order to save the significant time and resources spent on the trial-and-error process, some researchers started to predict tool shape using elastic theories. For example, Reuter [6] developed a model to predict the radius of a mold used in fabricating thin cylindrical panels. When released from the mold, the panels would deform to a predetermined curvature under the residual effect.

Our work also focuses on the design of the tool shape. The manufacturing of polymer composites involves complex interplay of heat transfer, curing, and residual stress development. Furthermore, tool material and design play a significant role in warpage and residual stress development [7]. In order to predict an accurate tool shape to achieve dimensional accuracy, we need a model to account for all these effects, as well as an efficient optimization scheme to systematically improve the design.

Our previous paper [2] presented a thermo-chemo-viscoelastic model for simulating the heat transfer, curing, residual stresses and deformation of composite parts over an entire cure cycle, i.e., the primal analysis of the problem. The model successfully predicted the process-induced warpage in cross-ply laminates and springforward in L-shaped composite parts. In this paper, we formalize the design process by integrating process modeling, design sensitivity analysis, and numerical optimization into a single framework. Design sensitivity analysis has been successfully applied in various optimization problems for material processing such as time-optimal cure cycle design for composite manufacturing [8] and optimal riser design for metal casting [9]. We are not aware of any applications of this method for shape optimization in thermo-chemo-viscoelastic problems.

All existing sensitivity analyses concerned with process-induced warpage in composites tend to rely on parametric studies. Johnston et al. [10] investigated the effects of composite thermophysical and mechanical properties as well as initial and boundary conditions on the warpage of a J-stiffened composite structure. Fernlund et al. [11] examined the sensitivities of the spring-in angles and web warpage of a composite spar to a series of parameters such as cross-section, toggle radius, flange length, heating rate, cure kinetics, cure shrinkage, etc. In this work, we use an analytical method for sensitivity computation, which utilizes the physical insight encapsulated in the primal analysis.

The paper is organized as follows: the next section briefly reviews the process model and its finite element implementation. Section 3 discusses the design sensitivity analysis and optimization scheme. The optimization results for two fundamental problems, i.e., mold design for cross-ply laminates and L-shaped composites parts, are presented in Sections 4 and 5. Finally, Section 6 summarizes this work.

## 2. THERMO-CHEMO-VISCOELASTIC ANALYSIS

The thermo-chemo-viscoelastic analysis of the manufacturing process has two main components. First, a thermochemical model is used to predict the temperature and cure history of each point in the part. A linear viscoelastic model is then used concurrently to calculate the thermal expansion–contraction and chemical shrinkage in the part, as well as the resulting residual stresses and deformation. This section briefly describes the basic formulations and finite element implementation of these two components. More details can be found in [2].

### 2.1 Thermochemical Model

The thermochemical model is described by

$$\rho c_p \frac{\partial T}{\partial t} = \frac{\partial}{\partial x_i} \left( k_{ij} \frac{\partial T}{\partial x_j} \right) + \rho H_R \frac{\partial c}{\partial t} \quad (i, j = 1, 2, 3) \quad (1)$$

$$\frac{\partial c}{\partial t} = G(T, c) \quad (2)$$

where  $\rho$  denotes the composite density,  $c_p$  the specific heat,  $T$  the temperature,  $k_{ij}$  the components of the thermal conductivity tensor,  $c$  the degree of cure defined as the ratio of the heat released by the reaction to the ultimate heat of reaction  $H_R$ , and  $G(T, c)$  represents some experimentally determined function of  $T$  and  $c$ .

The finite element formulation of the thermochemical problem can be written as

$$\mathbf{C}\dot{\mathbf{U}} + \mathbf{K}\mathbf{U} = \mathbf{P} \quad (3)$$

in which the vector  $\mathbf{U}$  contains the time-dependent nodal temperature and degree-of-cure values, and the coefficient matrices  $\mathbf{C}$ ,  $\mathbf{K}$ , and  $\mathbf{P}$  are calculated from the material thermal properties and the cure kinetics equation. The nonlinear coupled Equation (3) is solved using a conventional Newton–Raphson iterative scheme combined with the  $\beta$ -time stepping scheme.

## 2.2 Viscoelastic Stress Model

We assume that the material shows thermorheologically simple behavior at a constant degree of cure  $c_\beta$ , and is strain-free before  $t=0$ . The constitutive equation for an anisotropic linearly viscoelastic material can then be written as

$$\sigma_{ij}(t) = \int_0^t Q_{ijkl}(c_\beta, \chi - \chi') \frac{\partial}{\partial t'} (\varepsilon_{kl}(t') - \varepsilon_{kl}^{tc}(t')) dt' \quad (i, j, k, l = 1, 2, 3) \quad (4)$$

where  $\sigma_{ij}$  are the stress components,  $\varepsilon_{kl}$  the total strains,  $\varepsilon_{kl}^{tc}$  the free thermochemical strains,  $Q_{ijkl}$  the relaxation moduli, and  $\chi$  and  $\chi'$  the reduced times calculated from cure-dependent shift factor. The stress relaxation components in Equation (4) are approximated by  $M$  Maxwell elements as

$$Q_{ijkl}(c, \chi) = Q_{ijkl}^\infty(c) + Q_{ijkl}^*(c) \sum_{\omega=1}^M W_\omega(c) \exp\left(-\frac{\chi(c)}{\lambda_\omega(c)}\right) \quad (5)$$

where  $Q_{ijkl}^* = Q_{ijkl}^u - Q_{ijkl}^\infty$ ,  $Q_{ijkl}^\infty$  is related to the fully relaxed modulus (equilibrium modulus),  $Q_{ijkl}^u$  related to the unrelaxed modulus,  $W_\omega$  the weight factors, and  $\lambda_\omega$  the discrete relaxation times.

The finite element formulation of the viscoelastic model is developed starting from the variational theorem [12] for linear viscoelastic materials. Taylor's recursive scheme [13] is applied to overcome the difficulties of memory storage associated with the convolution relations (4). The resulting equations are linear relations in terms of the nodal displacement increment  $\Delta \mathbf{u}$  at time  $t_n$ ,

$$\hat{\mathbf{K}} \Delta \mathbf{u}(t_n) = \hat{\mathbf{F}}_1 + \hat{\mathbf{F}}_2 + \hat{\mathbf{F}}_3 \quad (6)$$

with

$$\hat{\mathbf{K}} = \mathbf{K}^\infty + \sum_{\omega=1}^M \mathbf{K}_\omega^* h_\omega(t_n) \quad (7)$$

$$\hat{\mathbf{F}}_1 = - \left[ \mathbf{K}^\infty \mathbf{u}(t_{n-1}) + \sum_{\omega=1}^M \mathbf{g}_\omega(t_n) \right] \quad (8)$$

$$\hat{\mathbf{F}}_2 = \mathbf{f}^\infty \boldsymbol{\epsilon}^{tc}(t_n) + \sum_{\omega=1}^M \mathbf{f}_\omega^* h_\omega(t_n) \Delta \boldsymbol{\epsilon}^{tc}(t_n) + \sum_{\omega=1}^M \mathbf{g}'_\omega(t_n) \quad (9)$$

$$\hat{\mathbf{F}}_3 = \int_{S_{lr}} \mathbf{N}^T T_{lr}(t_n) dS_{lr} \quad (10)$$

where  $\mathbf{g}_\omega(t_n)$  and  $\mathbf{g}'_\omega(t_n)$  are given recursively by

$$\mathbf{g}_\omega(t_n) = \exp\left(-\frac{\Delta \chi(t_n)}{\lambda_\omega}\right) [\mathbf{g}_\omega(t_{n-1}) + \mathbf{K}_\omega^* h_\omega(t_{n-1}) \Delta \mathbf{u}(t_{n-1})] \quad (11)$$

$$\mathbf{g}'_{\omega}(t_n) = \exp\left(-\frac{\Delta\chi(t_n)}{\lambda_{\omega}}\right) [\mathbf{g}'_{\omega}(t_{n-1}) + \mathbf{f}_{\omega}^* h_{\omega}(t_{n-1}) \Delta\epsilon^{tc}(t_{n-1})] \quad (12)$$

$\hat{\mathbf{K}}$  in Equation (6) denotes the stiffness matrix, and the load vector on the right-hand side consists of three components: the first component  $\hat{\mathbf{F}}_1$  is contributed by the previous displacement history; the second component  $\hat{\mathbf{F}}_2$  is associated with the thermochemical strain history; and the third component  $\hat{\mathbf{F}}_3$  is due to the current surface traction. Once the nodal displacement vector  $\mathbf{u}(t_n) = \mathbf{u}(t_{n-1}) + \Delta\mathbf{u}(t_n)$  is obtained, the stresses in each element are obtained by

$$\boldsymbol{\sigma}(t_n) = \mathbf{Q}^{\infty} \boldsymbol{\epsilon}^m(t_n) + \sum_{\omega=1}^M W_{\omega} \mathbf{Q}^* h_{\omega}(t_n) \Delta\boldsymbol{\epsilon}^m(t_n) + \sum_{\omega=1}^M \mathbf{g}''_{\omega}(t_n) \quad (13)$$

$$\mathbf{g}''_{\omega}(t_n) = \exp\left(-\frac{\Delta\chi t_n}{\lambda_{\omega}}\right) [\mathbf{g}''_{\omega}(t_{n-1}) + W_{\omega} \mathbf{Q}^* h_{\omega}(t_n) \Delta\boldsymbol{\epsilon}^m(t_{n-1})] \quad (14)$$

### 3. SENSITIVITY ANALYSIS AND OPTIMIZATION

To formulate an optimization problem one identifies a vector of design variables, a cost function, and constraints. The design variables represent the adjustable parameters of the problem within prescribed limits, the cost function is the objective to be minimized, and the constraints represent the physical and practical limitations of the process. In this study the cost function is defined as the difference between the final shape of a manufactured composite part and its desired shape.

To evaluate the cost and constraint functions for any given design vector requires one run of the primal analysis. The most efficient optimization schemes also need to know the derivatives of the cost and constraint functions with respect to the design variables, i.e., the design sensitivities. The key to effective optimization is to extract the design sensitivity information from the finite element primal analysis in a computationally efficient way. Rather than perturb the design variables one by one and make multiple analysis runs, we use the analytical sensitivity method. This method makes maximum use of the physical insight encapsulated in the primal analysis.

#### 3.1 Cost Function and Its Sensitivity

In this work the cost function is a function of the final displacement  $\mathbf{u}^n$  and design variables (geometrical variables)  $\mathbf{b}$ ,

$$F(\mathbf{b}) = f(\mathbf{u}^n(\mathbf{b}, \mathbf{U}^n, \mathbf{U}^{n-1}), \mathbf{b}) \quad (15)$$

where  $\mathbf{u}^n$  denotes the nodal displacement vector at the final time  $t_n$ , and depends on the design variables  $\mathbf{b}$ , nodal temperatures and degree of cures  $\mathbf{U}^n$  and  $\mathbf{U}^{n-1}$  at time  $t_n$  and  $t_{n-1}$ , respectively. The sensitivity expression is obtained by differentiating Equation (15) with

respect to each component  $b_i$  of  $\mathbf{b}$ ,

$$\frac{dF}{db_i} = \frac{\partial f}{\partial \mathbf{u}^n} \frac{d\mathbf{u}^n}{db_i} + \frac{\partial f}{\partial b_i} = \frac{\partial f}{\partial \mathbf{u}^n} \frac{\partial \mathbf{u}^n}{\partial b_i} + \frac{\partial f}{\partial \mathbf{u}^n} \frac{\partial \mathbf{u}^n}{\partial \mathbf{U}^n} \frac{d\mathbf{U}^n}{db_i} + \frac{\partial f}{\partial \mathbf{u}^n} \frac{\partial \mathbf{u}^n}{\partial \mathbf{U}^{n-1}} \frac{d\mathbf{U}^{n-1}}{db_i} + \frac{\partial f}{\partial b_i} \quad (16)$$

To solve for Equation (16) requires differentiation of both the nonlinear coupled thermochemical Equation (3) and the recursive viscoelastic Equation (6). To simplify the differentiation process, we assume that the dependence of the thermochemical field on small changes in the geometry are of second order compared to that of the displacement fields:

$$\frac{d\mathbf{U}^n}{db_i} \approx 0, \quad \frac{d\mathbf{U}^{n-1}}{db_i} \approx 0 \quad (17)$$

For thin laminates, this assumption is particularly justified since the temperature and degree of cure are almost uniform during the manufacturing process [2]. Obviously, the geometry of the part has almost no influence on the thermochemical fields in this case.

For thick composite parts, the temperature and degree-of-cure distributions are nonuniform due to the presence of thermal spike. Several cases have been studied to examine the change of geometry of thick composite parts on the thermochemical field. Figure 1 presents the evolution of the temperature and degree of cure at two locations in two 4-cm-thick parts with different curvature. Points C and D in the straight part correspond to points A and B of the same location in the curved-shape part, respectively. Both parts are subjected to a 5-h typical cure cycle involving a 1-h dwell at 120°C and a 2-h dwell at 177°C. The heating and cooling rates are approximately 2.5°C/min. Prescribed temperature boundary conditions along all domain boundaries are used in this study, except for the symmetry plane indicated in Figure 1. The material for both parts are chosen to be AS4/3501-6 graphite-epoxy, and its thermal properties and cure kinetics constants can be found in [2]. As apparent in Figure 1, the evolution of temperature and degree of cure at point A is almost the same as that at point C, and a similar phenomenon is observed for points B and D, confirming assumption (17). It is worth noting that before doing optimization for a concrete problem, we should carefully examine the validation of this assumption.

Under assumption (17), Equation (16) simplifies to

$$\frac{dF}{db_i} \approx \frac{\partial f}{\partial \mathbf{u}^n} \frac{d\mathbf{u}^n}{db_i} + \frac{\partial f}{\partial b_i} \quad (18)$$

in which the derivatives  $\partial f/\partial \mathbf{u}^n$  and  $\partial f/\partial b_i$  are determined explicitly from the definition of the cost function [Equation (15)], whereas the response sensitivity  $d\mathbf{u}^n/db_i$  is implicitly defined through the viscoelastic Equation (6). Several methods have been proposed to evaluate this sensitivity [14–16], namely, adjoint methods and the direction differentiation method. The latter method is used in this work.

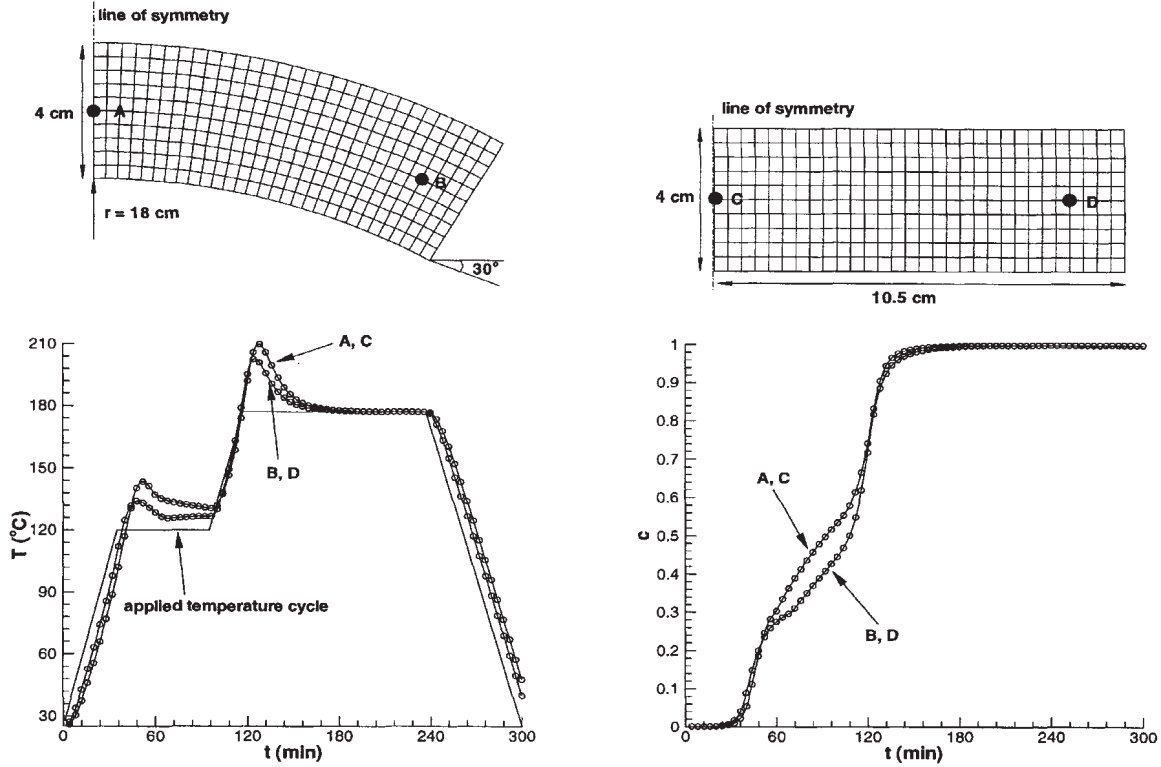


**Figure 1.** Evolution of the temperature (bottom left) and degree of cure (bottom right) computed at points A and B in a curved-shape part (top left) and at points C and D in a straight part (top right). The solid curves denote the values at points A and B, and the symbols denote the values at C and D.

In the direct differentiation method, Equation (6) is differentiated with respect to individual variable,  $b_i$  as

$$\hat{\mathbf{K}} \frac{d\Delta \mathbf{u}^n}{db_i} = -\frac{d\hat{\mathbf{K}}}{db_i} \Delta \mathbf{u}^n + \frac{d\hat{\mathbf{F}}_1}{db_i} + \frac{d\hat{\mathbf{F}}_2}{db_i} + \frac{d\hat{\mathbf{F}}_3}{db_i} \tag{19}$$

Equation (19) forms a pseudo-problem for the evaluation of the response sensitivity  $d\Delta \mathbf{u}^n/db_i$ . Notice that the coefficient matrix  $\hat{\mathbf{K}}$  is already formed in the primal analysis, and decomposed after solving the primal problem at time step  $n$ . Thus, the evaluation of  $d\Delta \mathbf{u}^n/db_i$  at this stage merely requires the formation of the pseudo-load vector, followed by a back-substitution using the existing decomposed stiffness matrix, thereby saving a great amount of computational effort. Once  $d\Delta \mathbf{u}^n/db_i$  is known, we calculate  $d\mathbf{u}^n/db_i$  by the recursive relation

$$\frac{d\mathbf{u}^n}{db_i} = \frac{d\mathbf{u}^{n-1}}{db_i} + \frac{d\Delta \mathbf{u}^n}{db_i} \tag{20}$$

in which the derivative  $d\mathbf{u}^{n-1}/db_i$  is a known quantity obtained in a previous step. The response sensitivity  $d\mathbf{u}^n/db_i$  can then be substituted into Equation (18) to evaluate the cost function sensitivity  $df/db_i$ . The main task in evaluating sensitivity is to form the pseudo-load vector, i.e., the right-hand side of Equation (19). The computation of each term of the pseudo-load vector is discussed next.

### 3.1.1 TERM $d\hat{\mathbf{K}}/db_i \Delta \mathbf{u}^n$

The displacement increment vector  $\Delta \mathbf{u}^n$  has already been solved in the primal analysis at time step  $n$ . We compute  $d\hat{\mathbf{K}}/db_i$  by differentiating Equation (7) into

$$\frac{d\hat{\mathbf{K}}}{db_i} = \frac{d\mathbf{K}^\infty}{db_i} + \sum_{\omega=1}^M h_\omega(t_n) \frac{d\mathbf{K}_\omega^*}{db_i} \tag{21}$$

where

$$\mathbf{K}^\infty = \int_V \mathbf{B}^T \mathbf{Q}^\infty \mathbf{B} dV \tag{22}$$

$$\mathbf{K}_\omega^* = \int_V \mathbf{B}^T W_\omega \mathbf{Q}^* \mathbf{B} dV \tag{23}$$

$$h_\omega(t_n) = \frac{\lambda_\omega}{\Delta \chi(t_n)} \left[ 1 - \exp\left(-\frac{\Delta \chi(t_n)}{\lambda_\omega}\right) \right] \tag{24}$$

$\mathbf{B}$  contains partial derivatives of the shape functions  $\mathbf{N}$  with respect to position vector  $\mathbf{X}$ , and  $\mathbf{Q}^\infty$  and  $\mathbf{Q}^*$  correspond to the element stiffness matrices computed from the relaxation moduli of the composite material. Note that in the preceding equations, the weight factor  $W_\omega$  is a material property and  $h_\omega$  only depends on the material relaxation and reduced times, thus both of them do not change with geometry. Also notice that since Equations (22) and (23) are in similar forms,  $d\mathbf{K}_\omega^\infty/db_i$  and  $d\mathbf{K}_\omega^*/db_i$  can be calculated in the same manner.

At the numerical level, isoparametric mapping in finite element method is used to integrate Equations (22) and (23). We transform the integration from the actual body domain ( $x$ - $y$ - $z$  system) to the reference domain ( $\xi$ - $\eta$ - $\zeta$  system), and express Equation (22) as

$$\mathbf{K}^\infty = \int_{-1}^1 \int_{-1}^1 \int_{-1}^1 \mathbf{B}^T \mathbf{Q}^\infty \mathbf{B} |\mathbf{J}| d\xi d\eta d\zeta \quad (25)$$

where  $|\mathbf{J}|$  is the determinant of Jacobian matrix  $\mathbf{J}$ . The advantage of the integration on the reference domain is that the reference element volume is a constant, and does not change with the actual body geometry, namely, with the design variable  $\mathbf{b}$ . To simplify the notation, we suppress the integral and rewrite Equation (25) in a compact way as

$$\mathbf{K}^\infty = \mathbf{B}^T \mathbf{Q}^\infty \mathbf{B} |\mathbf{J}| \quad (26)$$

Differentiation of Equation (26) gives

$$\frac{d\mathbf{K}^\infty}{db_i} = \frac{d\mathbf{B}^T}{db_i} \mathbf{Q}^\infty \mathbf{B} |\mathbf{J}| + \mathbf{B}^T \frac{d\mathbf{Q}^\infty}{db_i} \mathbf{B} |\mathbf{J}| + \mathbf{B}^T \mathbf{Q}^\infty \frac{d\mathbf{B}}{db_i} |\mathbf{J}| + \mathbf{B}^T \mathbf{Q}^\infty \mathbf{B} \frac{d|\mathbf{J}|}{db_i} \quad (27)$$

In the preceding equation,  $\mathbf{Q}^\infty$  is the material stiffness matrix defined in the global coordinate system. Suppose that two rotation angles  $\phi$  and  $\theta$  can be used to define the fiber orientation, then  $\mathbf{Q}^\infty$  is related to the on-axis stiffness matrix  $\bar{\mathbf{Q}}^\infty$  by

$$\mathbf{Q}^\infty = \mathbf{T}_\phi \mathbf{T}_\theta \bar{\mathbf{Q}}^\infty \mathbf{T}_\theta^{-1} \mathbf{T}_\phi^{-1} \quad (28)$$

where  $\mathbf{T}_\phi$  and  $\mathbf{T}_\theta$  are transformation matrices and also are used in Equation (39). Differentiation of Equation (28) yields

$$\begin{aligned} \frac{d\mathbf{Q}^\infty}{db_i} &= \frac{d\mathbf{T}_\phi}{db_i} \mathbf{T}_\theta \bar{\mathbf{Q}}^\infty \mathbf{T}_\theta^{-1} \mathbf{T}_\phi^{-1} + \mathbf{T}_\phi \frac{d\mathbf{T}_\theta}{db_i} \bar{\mathbf{Q}}^\infty \mathbf{T}_\theta^{-1} \mathbf{T}_\phi^{-1} \\ &+ \mathbf{T}_\phi \mathbf{T}_\theta \bar{\mathbf{Q}}^\infty \frac{d\mathbf{T}_\theta^{-1}}{db_i} \mathbf{T}_\phi^{-1} + \mathbf{T}_\phi \mathbf{T}_\theta \bar{\mathbf{Q}}^\infty \mathbf{T}_\theta^{-1} \frac{d\mathbf{T}_\phi^{-1}}{db_i} \end{aligned} \quad (29)$$

To compute the derivatives of  $\mathbf{T}_\phi$  and  $\mathbf{T}_\theta$ , we need the values of  $d\phi/db_i$  and  $d\theta/db_i$ , which are directly extracted from the chosen geometry.

The derivation of  $d\mathbf{B}/db_i$ ,  $d\mathbf{B}^T/db_i$ , and  $d|\mathbf{J}|/db_i$  which will be used in Equation (27) follows the standard approach as described in [9]. Note that the computation of these derivatives requires the values of the so-called velocity field, i.e., the derivatives of the nodal coordinates with respect to design variables, which directly relate to the chosen geometry. The computation of the velocity fields and the derivatives of the fiber orientations for the problems to be studied later in this paper will be presented in Appendices A and B.

### 3.1.2 TERM $d\hat{\mathbf{F}}_1/db_i$

The second term,  $d\hat{\mathbf{F}}_1/db_i$ , in the pseudo-load vector is contributed by the previous displacement history. Differentiation of Equation (8) yields

$$\frac{d\bar{\mathbf{F}}_1}{db_i} = - \left[ \frac{d\mathbf{K}^\infty}{db_i} \mathbf{u}^{n-1} + \mathbf{K}^\infty \frac{d\mathbf{u}^{n-1}}{db_i} + \sum_{\omega=1}^M \frac{d\mathbf{g}_\omega(t_n)}{db_i} \right] \quad (30)$$

Here  $d\mathbf{K}^\infty/db_i$  has been derived earlier,  $\mathbf{u}^{n-1}$  and  $d\mathbf{u}^{n-1}/db_i$  are known quantities from the previous step, thus all we need to calculate is the derivative of the recursive term  $d\mathbf{g}_\omega(t_n)/db_i$ , which is obtained by differentiating the recursive relation (11) into

$$\frac{d\mathbf{g}_\omega(t_n)}{db_i} = \exp\left(-\frac{\Delta\chi t_n}{\lambda_\omega}\right) \left[ \frac{d\mathbf{g}_\omega(t_{n-1})}{db_i} + \frac{d\mathbf{K}_\omega^*}{db_i} h_\omega(t_{n-1}) \Delta\mathbf{u}^{n-1} + \mathbf{K}_\omega^* h_\omega(t_{n-1}) \frac{d\Delta\mathbf{u}^{n-1}}{db_i} \right] \quad (31)$$

### 3.1.3 TERM $d\hat{\mathbf{F}}_2/db_i$

The third term in the pseudo-load is associated with the thermochemical strain history, and is calculated with

$$\begin{aligned} \frac{d\hat{\mathbf{F}}_2}{db_i} &= \frac{d\mathbf{f}^\infty}{db_i} \boldsymbol{\epsilon}^{tc}(t_n) + \mathbf{f}^\infty \frac{d\boldsymbol{\epsilon}^{tc}(t_n)}{db_i} \\ &+ \sum_{\omega=1}^M \left[ \frac{d\mathbf{f}_\omega^*}{db_i} h_\omega(t_n) \Delta\boldsymbol{\epsilon}^{tc}(t_n) + \mathbf{f}_\omega^* h_\omega(t_n) \frac{d\Delta\boldsymbol{\epsilon}^{tc}(t_n)}{db_i} \right] + \sum_{\omega=1}^M \frac{d\mathbf{g}'_\omega(t_n)}{db_i} \end{aligned} \quad (32)$$

where

$$\mathbf{f}^\infty = \int_V \mathbf{B}^T \mathbf{Q}^\infty dV, \quad \mathbf{f}_\omega^* = \int_V \mathbf{B}^T W_\omega \mathbf{Q}^* dV \quad (33)$$

The approach of evaluating  $d\mathbf{f}^\infty/db_i$  and  $d\mathbf{f}_\omega^*/db_i$  is similar to what we did earlier for  $d\mathbf{K}^\infty/db_i$ . The derivatives of the thermochemical strain are calculated by

$$\frac{d\boldsymbol{\epsilon}^{tc}(t_n)}{db_i} = \frac{d\mathbf{T}_\phi}{db_i} \mathbf{T}_\theta \bar{\boldsymbol{\epsilon}}^{tc}(t_n) + \mathbf{T}_\phi \frac{d\mathbf{T}_\theta}{db_i} \bar{\boldsymbol{\epsilon}}^{tc}(t_n) \quad (34)$$

where  $\bar{\boldsymbol{\epsilon}}^{tc}(t_n)$  is on-axis thermochemical strain. Finally,  $d\mathbf{g}'_\omega(t_n)/db_i$  is computed by differentiating Equation (12) into

$$\frac{d\mathbf{g}'_\omega(t_n)}{db_i} = \exp\left(-\frac{\Delta\chi t_n}{\lambda_\omega}\right) \left[ \frac{d\mathbf{g}'_\omega(t_{n-1})}{db_i} + \frac{d\mathbf{f}_\omega^*}{db_i} h_\omega(t_{n-1}) \boldsymbol{\epsilon}^{tc}(t_{n-1}) + \mathbf{f}_\omega^* h_\omega(t_{n-1}) \frac{d\boldsymbol{\epsilon}^{tc}(t_{n-1})}{db_i} \right] \quad (35)$$

### 3.1.4 TERM $d\hat{\mathbf{F}}_3/db_i$

The last term in the pseudo-load vector,  $d\hat{\mathbf{F}}_3/db_i$ , is contributed by the surface traction  $T_{ir}(t_n)$  at time step  $n$ . Differentiation of Equation (10) in the reference

domain gives

$$\frac{d\hat{\mathbf{F}}_3}{db_i} = \int_{A_{tr}} \left[ \mathbf{N}^T \frac{dT_{tr}(t)}{db_i} j + \mathbf{N}^T T_{tr}(t) \frac{dj}{db_i} \right] dA_{tr} \quad (36)$$

In the above equation,  $A_{tr}$  represents the surface in the reference domain which corresponds to the surface  $S_{tr}$  in the body domain where the traction is applied,  $j$  represents the change between the element areas in the reference domain and in the body domain, and  $dT_{tr}(t)/db_i$  is determined from the specific problem under consideration. For derivation of  $dj/db_i$ , see [9].

### 3.2 Residual Stress Constraint and Its Sensitivity

In addition to their detrimental effect on the dimensional accuracy, residual stresses can also influence the mechanical performance of composite parts by introducing micro-cracking in the matrix or even delamination. The residual stress constraint expresses the fact that, in order not to cause severe material degradation, the maximum stress developed during the manufacturing process must not exceed some allowable value, for example, material strength. This constraint is expressed by some function of stress vector  $\bar{\boldsymbol{\sigma}}$  in material principal directions as

$$g(\bar{\boldsymbol{\sigma}}) \leq 0 \quad (37)$$

The concrete form of  $g(\bar{\boldsymbol{\sigma}})$  depends on the strength criterion we choose. The constraint sensitivity is then obtained by differentiating Equation (37) with respect to individual design variables  $b_i$ , i.e.,

$$\frac{dg}{db_i} = \frac{\partial g}{\partial \bar{\boldsymbol{\sigma}}} \frac{d\bar{\boldsymbol{\sigma}}}{db_i} \quad (38)$$

The derivative  $\partial g/\partial \bar{\boldsymbol{\sigma}}$  is determined explicitly from the definition of  $g$ , whereas  $d\bar{\boldsymbol{\sigma}}/db_i$  is computed as follows.

The relation between the stresses  $\bar{\boldsymbol{\sigma}}$  in material principal directions and the stresses  $\boldsymbol{\sigma}$  in global coordinate system is

$$\bar{\boldsymbol{\sigma}} = \mathbf{T}_\theta^{-1} \mathbf{T}_\phi^{-1} \boldsymbol{\sigma} \quad (39)$$

Differentiation of the above equation gives

$$\frac{d\bar{\boldsymbol{\sigma}}}{db_i} = \frac{d\mathbf{T}_\theta^{-1}}{db_i} \mathbf{T}_\phi^{-1} \boldsymbol{\sigma} + \mathbf{T}_\theta^{-1} \frac{d\mathbf{T}_\phi^{-1}}{db_i} \boldsymbol{\sigma} + \mathbf{T}_\theta^{-1} \mathbf{T}_\phi^{-1} \frac{d\boldsymbol{\sigma}}{db_i} \quad (40)$$

To evaluate  $d\boldsymbol{\sigma}/db_i$ , we differentiate the aforementioned discrete version of the viscoelastic constitutive Equation (13) into

$$\begin{aligned} \frac{d\boldsymbol{\sigma}(t_n)}{db_i} &= \frac{d\mathbf{Q}^\infty}{db_i} \boldsymbol{\epsilon}^m(t_n) + \mathbf{Q}^\infty \frac{d\boldsymbol{\epsilon}^m(t_n)}{db_i} \\ &+ \sum_{\omega=1}^M \left[ \frac{d\mathbf{Q}^*}{db_i} h_\omega(t_n) \Delta \boldsymbol{\epsilon}^m(t_n) + \mathbf{Q}^* h_\omega(t_n) \frac{d\Delta \boldsymbol{\epsilon}^m(t_n)}{db_i} \right] + \sum_{\omega=1}^M \frac{d\mathbf{g}''_\omega(t_n)}{db_i} \end{aligned} \quad (41)$$

All the terms on the right-hand side of Equation (41) are known, except  $d\boldsymbol{\epsilon}^m(t_n)/db_i$ ,  $d\Delta \boldsymbol{\epsilon}^m(t_n)/db_i$  and  $d\mathbf{g}''_\omega(t_n)/db_i$ . The first one,  $d\boldsymbol{\epsilon}^m(t_n)/db_i$ , is computed by

$$\frac{d\boldsymbol{\epsilon}^m(t_n)}{db_i} = \frac{d\boldsymbol{\epsilon}(t_n)}{db_i} - \frac{d\boldsymbol{\epsilon}^{tc}(t_n)}{db_i} \quad (42)$$

where  $\boldsymbol{\epsilon}^m(t_n)$  is the mechanical strain vector,  $\boldsymbol{\epsilon}(t_n)$  is the total strain vector defined by

$$\boldsymbol{\epsilon}(t_n) = \mathbf{B}\mathbf{u}^n \quad (43)$$

Substituting Equation (43) into Equation (42), we have

$$\frac{d\boldsymbol{\epsilon}^m(t_n)}{db_i} = \frac{d\mathbf{B}}{db_i} \mathbf{u}^n + \mathbf{B} \frac{d\mathbf{u}^n}{db_i} - \frac{d\boldsymbol{\epsilon}^{tc}(t_n)}{db_i} \quad (44)$$

All the terms on the right-hand side of the preceding equation have been calculated in the evaluation of the sensitivity of the objective function. Once  $d\boldsymbol{\epsilon}^m(t_n)/db_i$  is available, it is easy to obtain  $d\Delta \boldsymbol{\epsilon}^m(t_n)/db_i$ . The derivative of the recursive term  $d\mathbf{g}''_\omega(t_n)/db_i$  is calculated by substituting the previous results into the following equation:

$$\frac{d\mathbf{g}''_\omega(t_n)}{db_i} = \exp\left(-\frac{\Delta \chi t_n}{\lambda_\omega}\right) \left[ \frac{d\mathbf{g}''_\omega(t_{n-1})}{db_i} + \frac{d\mathbf{Q}^*}{db_i} h_\omega(t_n) \Delta \boldsymbol{\epsilon}^m(t_{n-1}) + \mathbf{Q}^* h_\omega(t_n) \frac{d\Delta \boldsymbol{\epsilon}^m(t_{n-1})}{db_i} \right] \quad (45)$$

The sensitivity of this constraint is evaluated only for the maximum value of  $g(\bar{\boldsymbol{\sigma}})$  occurring in the domain over the entire cure cycle. If at a time step, the maximum value among all the elements is larger than the maximum before that time step, this constraint sensitivity is computed and updated at that particular time step. If all the values of  $g(\bar{\boldsymbol{\sigma}})$  in the domain are less than the maximum before that time step, this constraint sensitivity retains the same value evaluated before.

Besides the residual stress constraint, the shape design of a composite part may also be subjected to other limitations such as stiffness requirements, material cost, manufacturing difficulties, etc. These constraints are defined in different ways for different problems, but most of them can be added to the code easily.

### 3.3 Optimization

The sensitivity analysis has been implemented with the 2-D plane-strain finite element scheme. As indicated earlier, the response sensitivities are computed concurrently with the transient primal analysis. At each time step, the pseudo-load vectors associated with each

design variable are formed, and the response sensitivities are computed by back-substitution into the decomposed stiffness matrix used in the primal analysis. At the end of the cure cycle, the cost and constraint functions and the design sensitivities are computed and provided to an optimization code, Design Optimization Tools (DOT) [17]. For unconstrained problems, DOT uses the Broydon-Fletcher-Goldfarb-Shanno optimization algorithm. For constrained optimization problems, the option of the optimization algorithm is set to sequential quadratic programming method.

#### 4. MOLD DESIGN FOR LAMINATES WITH DESIRED CURVATURE

Flat and cylindrical laminates are widely used in engineering applications. These laminates are fabricated by stacking precut prepregs over a rigid, flat or cylindrical mold segment followed by a cure cycle. Residual stresses develop in the laminate during the processing, which sometimes results in a noticeable and potentially troublesome distortion upon the laminate releasing from the mold (tool). This problem is especially acute in unsymmetric layups. The final curvature of the laminate is often quite different from that of the tool. Our previous study [2] showed excellent correlation between the numerical and experimental curvatures for thin cross-ply laminates. The objective of this sequel study is to determine the shape of the mold needed to fabricate composite laminates with prescribed curvature in a hot press curing.

One design variable, the mold surface curvature  $\kappa$ , is selected to characterize the mold shape. The cost function is defined as the absolute difference between the desired curvature  $\kappa_d$  and the final curvature  $\kappa_f$  of the laminate,

$$F = |\kappa_d - \kappa_f| \quad (46)$$

with  $\kappa_f$  determined by [18]

$$\kappa_f = 2h/(l^2/4 + h^2) \quad (47)$$

In the preceding equation,  $h$  and  $l$  denote the warped laminate height and length (Figure 2), respectively, and are readily calculated from nodal coordinates and displacements. In this study only side constraints, i.e., upper and lower bounds, on the design variable are considered as described later in this section.

Before running a shape optimization analysis, the velocity field for the chosen geometry needs to be known. If the material is composite, the derivatives of the fiber orientation with respect to the design variable to be used in Equations (29) and (34) also need to be evaluated. This information is provided to the code to compute the response sensitivities. In this problem an analytical method is used to calculate these derivatives (Appendix A).

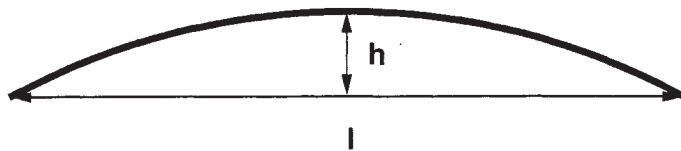
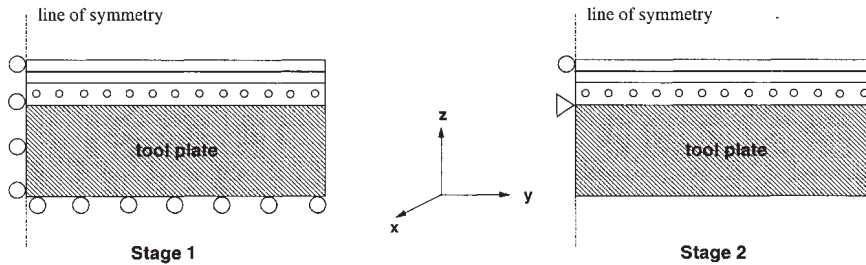


Figure 2. Determination of the curvature of a warped laminate.



**Figure 3.** Two stages in the simulation of the cross-ply laminates. Half of the laminate is analyzed due to symmetry.

We first consider a mold design for manufacturing a flat AS4/3501-6 graphite–epoxy laminate, namely,  $\kappa_d = 0$ . To emphasize the residual stress effect, we choose a  $[0/90]$  layup, i.e., the fibers are perpendicular to the laminate cross-section in the bottom plies, and parallel to the cross-section in the top plies. In our plane-strain model, the thickness and length of the laminate are 1 and 40 mm, respectively, and the mold is 5 mm thick in the middle plane. Eight-node quadrilateral elements are used in this study. The simulation process is divided into two stages (Figure 3). In the first stage, the laminate is placed in the mold and subjected to the same temperature cycle as described in Section 3.1. Prescribed temperature conditions are applied on all domain boundaries, except for the symmetry line. Perfect bonding is assumed between the laminate and the bottom mold, and free boundary condition is used along the top surface. The first stage of the process ends by cooling the laminate back to room temperature. In the second stage of the simulation, the laminate is released from the mold at room temperature. The part release process is simulated numerically by releasing the mechanical constraints at the bottom of the tool plate. The Young's modulus of the tool is then set to a very small value (approximately six orders of magnitude smaller than the original value) to allow the process-induced warpage to take place. The properties of the graphite–epoxy composite and the steel mold can be found in [2].

The optimization process starts from an initial design curvature  $\kappa = 0$ , which is equal to the laminate desired curvature. Obviously, to reach a flat shape, the mold surface should be curved upwards to offset the process-induced downwards curvature in the laminate. The lower and upper bounds of the design variable are set to 0 and  $15 \text{ m}^{-1}$ , respectively. The optimization program evaluates the cost function 14 times and its sensitivity three times until the mold curvature converges to  $3.154 \text{ m}^{-1}$ . This magnitude is smaller than that of the final curvature,  $-3.204 \text{ m}^{-1}$  (the negative sign indicates that the laminate is curved downwards), induced in an initially flat laminate.

The development of transverse stress  $\sigma_y$  in the bottom ply at the center of the laminate is plotted in Figure 4. The evolution of the residual transverse stress in the laminate obtained with the initial and optimal mold designs is very similar. At the beginning of the cure cycle, a compressive stress appears due to the temperature increase. Later on, as the material progressively cures, a tensile stress arises from the chemical shrinkage. The residual stress reaches its maximum value at the end of the cure cycle, after the part is cooled down to room temperature. Once the laminate is released from the mold, about 50% of the residual stress is released through the warpage of the composite laminate. A similar pattern and magnitude of residual stresses between initial and optimal designs are expected: since the warpage here is only caused by the thermal and chemical expansion mismatch between

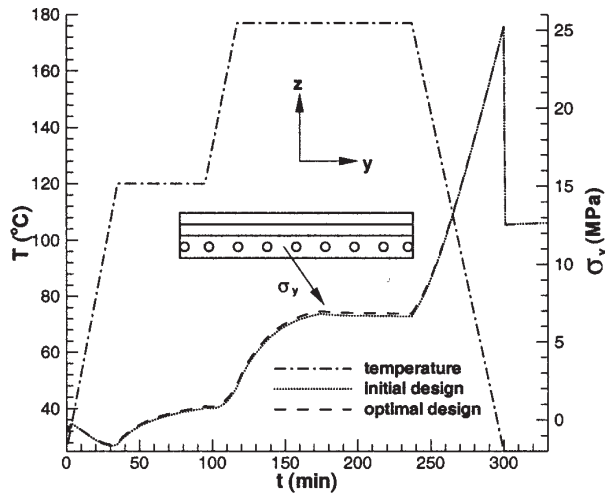


**Figure 4.** Temperature cycle and residual stress  $\sigma_y$  development in the bottom ply at the center of the laminate.

[0] and [90] plies, a small change in curvature has little effect on the residual stress development. Therefore, for this particular problem, the introduction of a stress constraint is not justified.

We now turn our attention to the design of molds with different coefficients of thermal expansion (CTE). To emphasize the role of the mold CTE, the stiffness of the mold material is kept constant (equal to that of steel), but the mold CTE is systematically varied. A mold with a flat surface, higher CTE  $\alpha_{\text{mold}} = 25 \times 10^{-6} \text{°C}^{-1}$ , produces a curvature of  $-2.799 \text{ m}^{-1}$  in the laminate. This value is approximately 13% smaller than the warpage with the previously studied mold, for which  $\alpha_{\text{mold}} = 12 \times 10^{-6} \text{°C}^{-1}$ . This phenomenon can be explained from Figure 5, which reveals the strong effect of mold CTE on the residual stress development in the laminate. Before the cooldown, the deformation of the tool is due to thermal expansion, while the deformation of the laminate is dominated by the cure shrinkage. The stretching of the bottom ply by the expanding tool results in tensile stress in the bottom ply. Thus, the higher the tool CTE, the higher the tensile stress. During the cooldown, the bottom ply shrinks more than the tool due to its higher CTE ( $35.3 \times 10^{-6} \text{°C}^{-1}$ ). Thus, the smaller the tool-composite CTE mismatch, the lower the residual stress. The resulting total residual stress in the bottom ply at the end of the cure cycle and the final warpage of the laminate decrease as the mold CTE increases from 0 to  $25 \times 10^{-6} \text{°C}^{-1}$ . Accordingly, the optimal design curvature of a mold with  $\alpha_{\text{mold}} = 25 \times 10^{-6} \text{°C}^{-1}$  is smaller than that of a steel mold, while a mold for which  $\alpha_{\text{mold}} = 0 \text{°C}^{-1}$  has the largest optimal design curvature (Table 1).

Next, we study a mold design for manufacturing a 1 mm-thick [0/90] AS4/3501-6 graphite-epoxy cylindrical laminate with a desired curvature  $\kappa_d = 10 \text{ m}^{-1}$ . The results of this study are summarized in Table 2, and yield similar conclusions to the flat laminate case. The optimal design curvature for a steel mold is  $13.004 \text{ m}^{-1}$ , and the difference between the optimal and desired curvatures is smaller than the curvature ( $-3.049 \text{ m}^{-1}$ ) in a laminate with an initial mold design of  $\kappa = 10 \text{ m}^{-1}$ . The optimal design curvature increases when the mold CTE decreases.

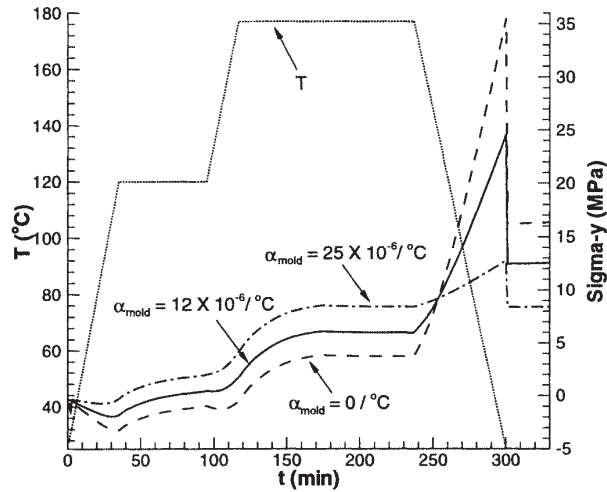


**Figure 5.** Effect of mold CTE on the development of the residual stress  $\sigma_y$  in the bottom ply at the center of the cross-ply laminate.

**Table 1.** Mold design for a 1 mm-thick flat laminate ( $\kappa_d = 0$ ).

Mold Thermal Expansion $\alpha_{\text{mold}} (\times 10^{-6} \text{ } ^\circ\text{C}^{-1})$	Mold Curvature $\kappa (\text{m}^{-1})$	Final Curvature $\kappa_f (\text{m}^{-1})$	Cost Function Value $ \kappa_d - \kappa_f  (\text{m}^{-1})$
0	0 (initial)	-3.578	3.578
0	3.520 (optimal)	0.000	$1.190 \times 10^{-20}$
12	0 (initial)	-3.204	3.204
12	3.154 (optimal)	0.000	$7.462 \times 10^{-18}$
25	0 (initial)	-2.799	2.799
25	2.758 (optimal)	0.000	$2.947 \times 10^{-20}$

**Table 2.** Mold design for a 1 mm-thick cylindrical laminate ( $\kappa_d = 10 \text{ m}^{-1}$ ).

Mold Thermal Expansion $\alpha_{\text{mold}} (\times 10^{-6} \text{ } ^\circ\text{C}^{-1})$	Mold Curvature $\kappa (\text{m}^{-1})$	Final Curvature $\kappa_f (\text{m}^{-1})$	Cost Function Value $ \kappa_d - \kappa_f  (\text{m}^{-1})$
0	0 (initial)	6.585	3.415
0	13.360 (optimal)	10.000	$2.399 \times 10^{-21}$
12	10 (initial)	6.951	3.049
12	13.004 (optimal)	10.000	$1.201 \times 10^{-19}$
25	10 (initial)	7.346	2.654
25	12.619 (optimal)	10.000	$1.463 \times 10^{-21}$

## 5. MOLD DESIGN FOR L-SHAPED COMPOSITE PARTS

Another important effect of process-induced residual stresses on the dimensional accuracy of composites is the springforward phenomenon: If a composite part has a bend, the included angle in the final part will usually be smaller than the same angle in the tooling (Figure 6). This paper discusses the optimal mold design for fabricating L-shaped AS4/3501-6 graphite-epoxy composite parts with  $90^\circ$  enclosed angle. The mold angle  $\gamma$ ,

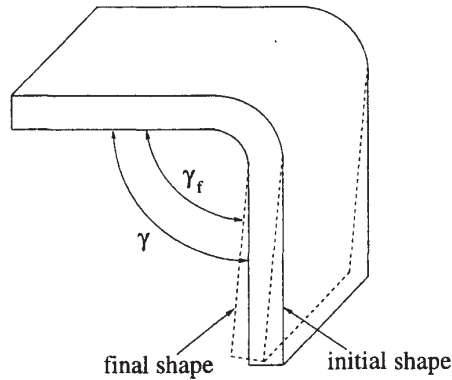


**Figure 6.** Springforward phenomenon in an L-shaped composite part.

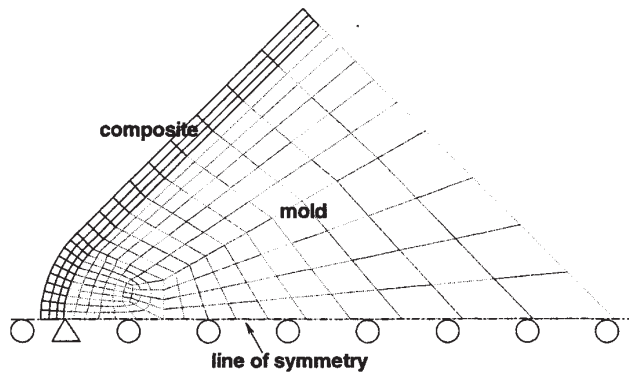


**Figure 7.** Finite element discretization for the 1.15 mm-thick L-shaped composite part, male mold and symmetry boundary condition.

which is also the initial enclosed angle of the layup, is chosen as the only design variable. The cost function is defined as the absolute difference between the final enclosed angle of the manufactured part  $\gamma_f$  and the desired angle  $\gamma_d = 90^\circ$ , i.e.,

$$F = |\gamma_d - \gamma_f| \quad (48)$$

The composite is made of a unidirectional layup, i.e., the fibers are oriented in the plane of the cross section. We first consider a 1.15 mm-thick part with an inner radius of 5 mm. The length of the straight section of the part is 16 mm. Taking advantage of symmetry, only one half of the part is modeled (Figure 7). Eight-node plane-strain isoparametric elements are used in this study. The composite part is placed in a steel male mold and undergoes the same temperature cycle as the thin laminate in the previous section. The laminate is assumed to be connected to the mold during the cure cycle, and no slip is allowed. Once the cure cycle is completed, the composite part is released from the mold and the springforward is obtained by calculating the change in angle of the straight portion of the laminate. It is worth mentioning that eventhough the part is unidirectional, some curvature could be formed in the straight portion due to the asymmetry introduced

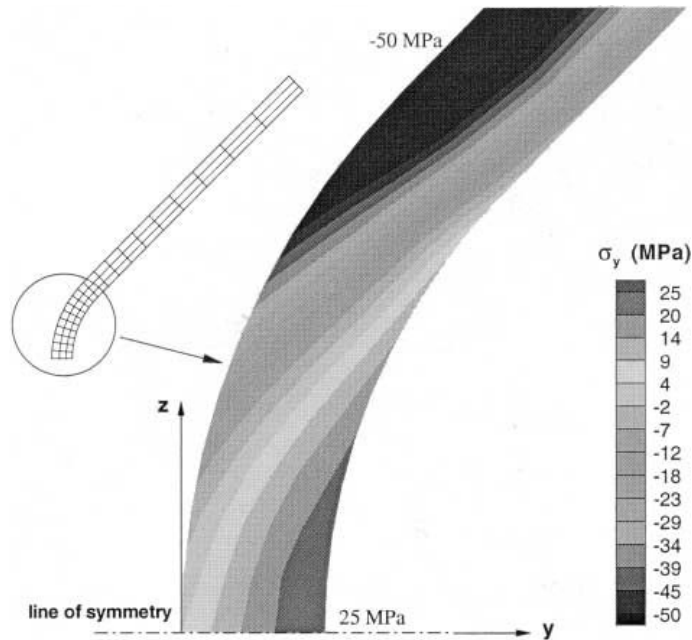


**Figure 8.** Residual stress  $\sigma_y$  distribution in a 1.15 mm-thick L-shaped composite part with the optimal mold design at the end of the cure cycle just before the part is released from the mold.

by the tool–part interaction. The numerical results indicate, however, that the curvature effect is very small compared to the springforward effect described in [2]. An analytical method is used to calculate the velocity field and derivatives of fiber orientation in the composite (Appendix B).

We start from an initial design of  $\gamma = 90^\circ$ , and set the lower and upper bounds of  $\gamma$  to be  $90^\circ$  and  $95^\circ$ , respectively. The optimization program evaluates the cost function nine times, and the design sensitivity three times, until the mold angle converges to  $\gamma = 92.233^\circ$ . The mold angle increment,  $2.233^\circ$ , is slightly smaller than the springforward,  $2.262^\circ$ , in an initial  $90^\circ$  layup. Figure 8 presents the distribution of residual stress,  $\sigma_y$ , in the curved section at the end of the cure cycle, just before the part is released from the mold. The maximum transverse stress, about 25 MPa, is observed in the center of the inner side of the curved section due to the restriction of the mold. Since the mold angle only increases a small amount, little difference is observed in the residual stress development between the initial and optimal design. When the mold CTE increases, the springforward as well as the optimal design angle also increases. As listed in Table 3, with a mold for which  $\alpha_{\text{mold}} = 25 \times 10^{-6} \text{C}^{-1}$ , the springforward in an initial design increases to  $3.616^\circ$ , and the optimal mold design angle increases to  $93.557^\circ$ .

As described in [19] and our previous study [2], the springforward decreases when the part thickness increases. This phenomenon can be explained by the concept of “tool-induced stretching,” which was also observed in [7]. To provide some insight on the origin of the thickness dependence of the springforward effect, we present, in Figure 9, the variation of the residual stress  $\sigma_z$  along the symmetry line of the composite part (see Figure 8 for the axis system definition). The residual stress obtained from a purely elastic analysis of the cooldown stage only (assuming stress-free initial conditions) is shown in Figure 9(a).

**Table 3. Male mold design for a 1.15 mm-thick L-shaped composite part.**

Mold Thermal Expansion $\alpha_{\text{mold}} (\times 10^{-6} \text{ } ^\circ\text{C}^{-1})$	Mold Angle $\gamma (\text{ } ^\circ)$	Final Angle $\gamma_f (\text{ } ^\circ)$	Cost Function Value $ \gamma_d - \gamma_f  (\text{ } ^\circ)$
0	90 (initial)	88.970	1.030
0	91.020 (optimal)	90.000	$1.029 \times 10^{-22}$
12	90 (initial)	87.728	2.262
12	92.233 (optimal)	90.000	$7.937 \times 10^{-18}$
25	90 (initial)	86.384	3.616
25	93.557 (optimal)	90.000	$1.372 \times 10^{-21}$

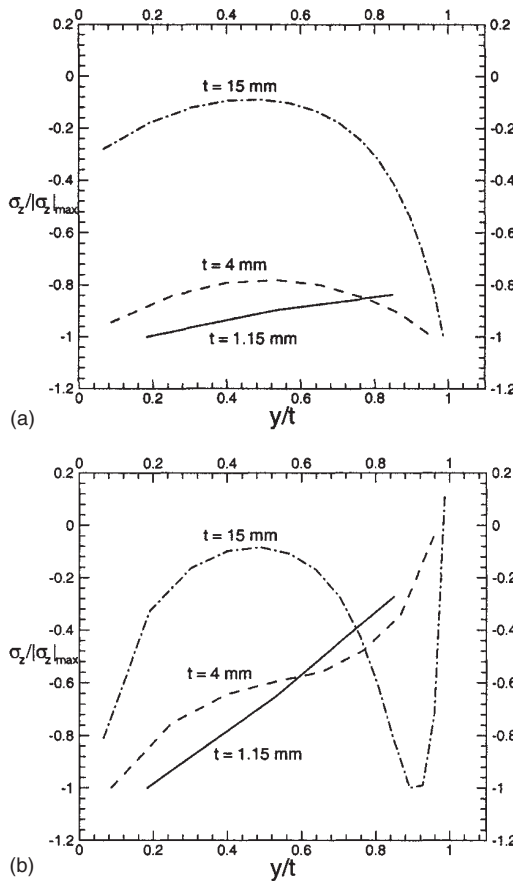


**Figure 9.** The effect of part thickness on the normalized residual stress  $\sigma_z / |\sigma_z|_{\text{max}}$  distribution along the symmetry line of the L-shaped composites just before they are released from the male mold.  $y = 0$  represents the outside (free side) boundary of the composite part,  $y = t$  represents the inside (tool side) boundary and  $t$  is the part thickness: (a) elastic model, cooldown stage only and (b) viscoelastic model, entire cure cycle.

It clearly illustrates the compressive effect of the mold (located at  $y = t$ ), especially for thicker specimens. As indicated in [2], in this elastic case, the resulting springforward is independent of the thickness and agrees with the results presented in [20]. The situation is quite different if the aforementioned cure- and temperature-dependent viscoelastic model

**Table 4. Male mold design for L-shaped composite parts with varying thicknesses (inner radius = 5 mm,  $\alpha_{\text{mold}} = 25 \times 10^{-6} \text{ }^\circ\text{C}^{-1}$ ).**

Part Thickness $t$ (mm)	Mold Angle $\gamma$ ( $^\circ$ )	Final Angle $\gamma_f$ ( $^\circ$ )	Cost Function Value $ \gamma_d - \gamma_f $ ( $^\circ$ )
1.15	90 (initial)	86.384	3.616
1.15	93.557 (optimal)	90.000	$1.372 \times 10^{-21}$
4	90 (initial)	88.646	1.354
4	91.341 (optimal)	90.000	$3.020 \times 10^{-18}$
15	90 (initial)	89.159	0.841
15	90.835 (optimal)	90.000	$6.914 \times 10^{-18}$

**Table 5. Male and female mold design for a 4 mm-thick L-shaped composite part ( $\alpha_{\text{mold}} = 25 \times 10^{-6} \text{ }^\circ\text{C}^{-1}$ ).**

Mold Design	Mold Angle $\gamma$ ( $^\circ$ )	Final Angle $\gamma_f$ ( $^\circ$ )	Cost Function Value $ \gamma_d - \gamma_f $ ( $^\circ$ )
Male mold	90 (initial)	88.945	1.055
Male mold	91.047 (optimal)	90.000	$1.286 \times 10^{-20}$
Female mold	90 (initial)	89.615	0.385
Female mold	90.382 (optimal)	90.000	$9.523 \times 10^{-22}$

is used to capture the material response throughout the cure cycle [Figure 9(b)]. Due to the chemical shrinkage in the composite part, the tool exerts a stretching effect which is felt in the vicinity of the tool–part interface. This stretching effect substantially reduces the compressive residual stress distribution near  $y = t$ . In the case of thicker composite parts,  $\sigma_z$  even becomes tensile in the vicinity of the tool. The extent of the stretching effect within the parts determines how much it affects the springforward angle: thinner parts tend to experience a larger springforward than thicker parts. Accordingly, the optimal mold angle differs from part to part with varying thicknesses (Table 4). For example, the optimal design angle of a mold for which  $\alpha_{\text{mold}} = 25 \times 10^{-6} \text{ }^\circ\text{C}^{-1}$  is  $93.557^\circ$  for fabricating a 1.15 mm-thick part, but decreases to  $90.835^\circ$  for a 15 mm-thick part.

Comparison is also made between steel male and female mold designs for a 4 mm-thick composite part (Table 5). The optimal angle ( $91.047^\circ$ ) of a male mold is larger than that of a female mold ( $90.382^\circ$ ) since a female mold results in a smaller springforward than a male counterpart. As indicated in [2], this result is due to the fact that the female mold exerts an aforementioned stretching effect on the outside layer of the laminate, thus decreasing the springforward effect. The same trend was observed in Huang and Yang's experiments [21], in which the springforward was found to be 21–62% smaller in a female mold than in a male mold with various mold angles.

## 6. SUMMARY

In this work, we have demonstrated the adequacy of numerical optimization techniques to systematically improve the tool shape design to achieve dimensional accuracy in manufacturing thermoset composites. Shape sensitivities have been formulated for the thermo-chemo-viscoelastic system using the direct differentiation method. Special emphasis has been placed on formulating the sensitivities of the displacements and residual

stresses with respect to the design variables. The change in design variables on the thermochemical field has been assumed to only have a second-order effect, and thereby was ignored.

The shape sensitivities are combined with process modeling and numerical optimization tool, DOT, to design molds for fabricating cross-ply laminates and L-shaped composite parts. The optimization results reveal that the mold plays an important role in the mold design. For manufacturing L-shaped composite parts, the optimal mold shape also differs with part thickness and mold design (male mold versus female mold). The results also indicate that a small change in the tool shape has little effect on the residual stress development, thereby rendering a stress constraint irrelevant in these cases. Therefore the maximum residual stress constraint did not apply in these two cases. However, this constraint may be important and can be utilized in other shape design problems. Besides the tool design, this approach can be extended to address other product quality issues, for example, the shape design of a hat-stiffener in the bond-line-read-out problem [22]. We will pursue these issues in a future publication.

The approach described in this paper is an efficient and accurate way to achieve dimensional accuracy in manufacturing thermoset composites. It is important to note, however, that this approach is not limited to this class of problems, and can also be used for a wide range of shape design problems involving viscoelastic materials.

## ACKNOWLEDGMENTS

This work was supported by the National Science Foundation, Grant No. DMI 96-10382. The authors wish to thank Professors C. L. Tucker III and S. R. White, and Mr. M. Li and D. J. O'Brien for helpful discussions.

## APPENDIX A

### Velocity Field for Curved Laminate and Mold

The computation of the velocity field, i.e., the derivatives of the nodal positions with respect to the design variable(s), is an essential component of the shape optimization scheme. We summarize here the velocity computation for the curved laminate problem described in Section 4. The laminate and tool geometry, and its finite element discretization are shown in Figure A-1 for two values of the curvature ( $\kappa=0$  and  $\kappa > 0$ ). Using the flat laminate and mold as reference, and assuming that the laminate thickness and the length of the bottom side of the laminate remain constant ( $AB=A'B'$  in Figure A-2), we can relate the coordinates of a node in the base geometry ( $x_0, y_0$ ) of the laminate to those in the actual geometry ( $x, y$ ) by

$$x = (R - y_0) \sin \phi, \quad y = R - (R - y_0) \cos \phi \quad (\text{A1})$$

with

$$R = \frac{1}{\kappa}, \quad \phi = \frac{x_0}{R} \quad (\text{A2})$$

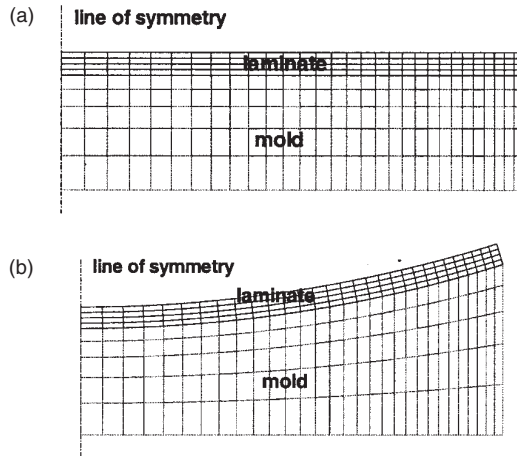


Figure A-1. Finite element discretization for: (a) flat ( $\kappa=0$ ) and (b) curved ( $\kappa=15\text{ m}^{-1}$ ) laminates and molds.

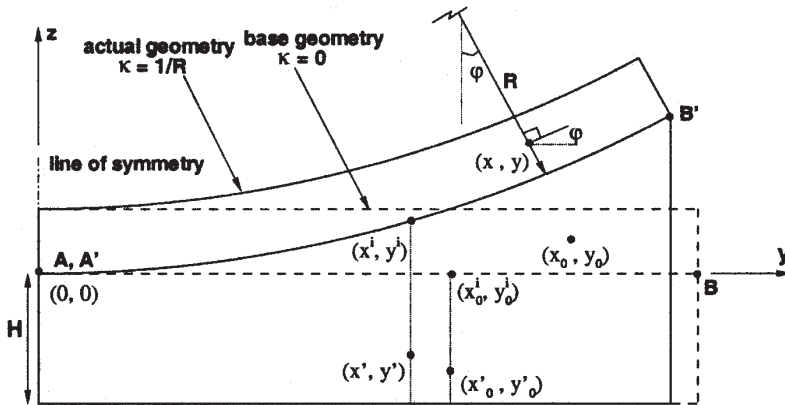


Figure A-2. Geometry of a curved laminate and mold.

Note that the numerical difficulties associated with the limiting case  $\kappa \rightarrow 0$  can be resolved through a Taylor series expansion of  $\sin \phi$  and  $\cos \phi$ .

To calculate the actual coordinates of a node from the original mold domain  $(x'_0, y'_0)$ , we begin with the node at the interface  $(x^i_0, y^i_0)$  with the same  $x$ -coordinate in the base geometry, i.e.,  $x^i_0 = x'_0$ . The coordinates of the same interfacial node in the actual geometry,  $(x^i, y^i)$ , are obtained by Equations (A1) and (A2).  $x'$  and  $y'$  are then calculated by

$$x' = x^i, \quad y' = \frac{y'_0 + H}{H} (y^i + H) - H \tag{A3}$$

The preceding equations express the fact that in the mold domain, the nodes on a vertical line in the base geometry remain on a vertical line in the actual geometry, and the distance from a node to the bottom side of the mold in the actual geometry is proportional to that in the base geometry.

As described in Equation (28), two rotation angles  $\phi$  and  $\theta$  characterize the fiber orientation in the composite. The dependence of  $\phi$  on the design variable  $\kappa$  is described by Equation (A2). In this particular problem, the angle  $\theta$  between the fibers and the direction of the normal to the composite cross section is independent of the mold curvature  $\kappa$ , i.e.,  $d\theta/d\kappa = 0$ .

The velocity field  $dx/d\kappa$ ,  $dy/d\kappa$ ,  $dx'/d\kappa$ ,  $dy'/d\kappa$  and the derivative of the fiber orientation with respect to the design variable  $d\phi/d\kappa$  are then evaluated by Equations (A1)–(A3).

### APPENDIX B

#### Velocity Field for L-Shaped Composite Part

The L-shaped composite part and mold geometries, and their finite element discretization are shown in Figures B-1 and B-2 for the cases of male and female molds, respectively. We take the composite part for which  $\gamma = 90^\circ$  as reference (Figure B-3), and assume that the thickness of the composite part, the inner radius of the curved portion, and the length of the composite part remain constant ( $AB = A'B'$  and  $CD = C'D'$  in Figure B-3).

In the curved portion, the coordinates of a node in the base geometry  $(x_0, y_0)$  are related to those in the actual geometry  $(x, y)$  by

$$x = -R \cos \tilde{\theta}, \quad y = R \sin \tilde{\theta} \tag{B1}$$

with

$$R = \sqrt{(x_0)^2 + (y_0)^2}, \quad \tilde{\theta} = \frac{\tilde{\theta}_0}{\pi/4} \frac{\pi - \gamma}{2}, \quad \tilde{\theta}_0 = \arctan\left(-\frac{y_0}{x_0}\right) \tag{B2}$$

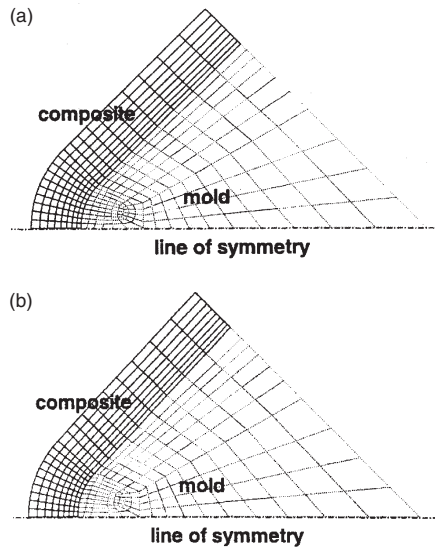


**Figure B-1.** Finite element discretization for 4 mm-thick L-shaped composite parts and male molds with: (a)  $\gamma = 90^\circ$  and (b)  $\gamma = 94^\circ$ .

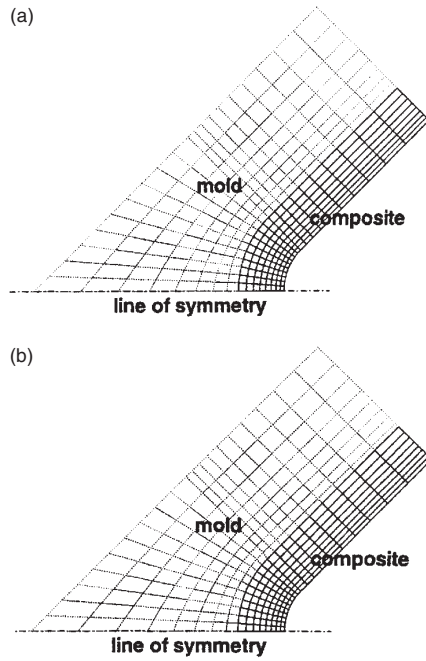


**Figure B-2.** Finite element discretization for 4 mm-thick L-shaped composite parts and female molds with: (a)  $\gamma=90^\circ$  and (b)  $\gamma=92^\circ$ .

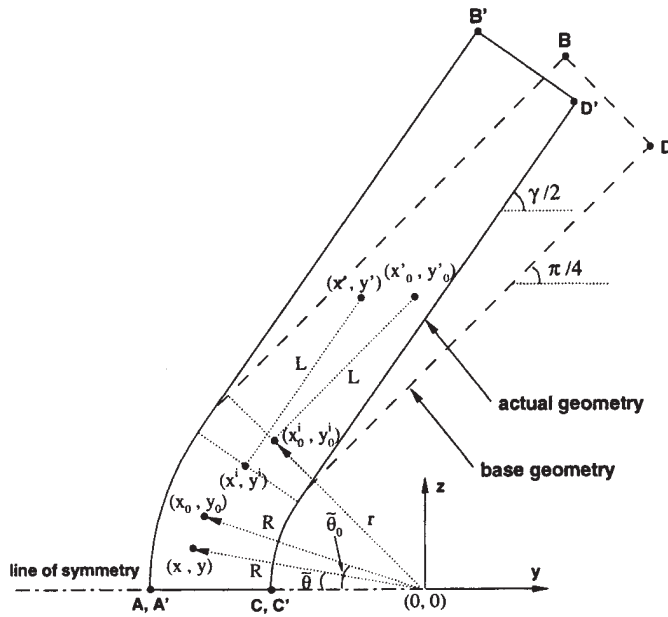


**Figure B-3.** Geometry of an L-shaped composite part.

To calculate the actual coordinates of a node in the straight portion with coordinates of  $(x'_0, y'_0)$  in the base geometry, we begin with its corresponding node  $(x_0^i, y_0^i)$  at the interface of the curved and straight portions. The line connecting these two nodes is parallel to the straight portion, and has a length of  $L$ . The actual coordinates  $(x^i, y^i)$  of the interfacial node are evaluated by Equations (B1)–(B2).  $(x', y')$  are then computed by

$$x' = x^i + L \cos(\gamma/2), \quad y' = y^i + L \sin(\gamma/2) \quad (\text{B3})$$

with

$$L = \sqrt{(x_0 - x_0^i)^2 + (y_0 - y_0^i)^2} + r(\gamma/2 - \pi/4), \quad r = \sqrt{(x_0^i)^2 + (y_0^i)^2} \quad (\text{B4})$$

The fiber orientation angle  $\phi$ , which corresponds to the angle between the fiber and the horizontal axis, is given by

$$\phi = \pi/2 - \tilde{\theta} \quad \text{at } (x, y), \quad \phi = \gamma/2 \quad \text{in straight portion} \quad (\text{B5})$$

The velocity field  $dx/d\gamma$ ,  $dy/d\gamma$ ,  $dx'/d\gamma$ ,  $dy'/d\gamma$  and the derivative of the fiber orientation with respect to the design variable  $d\phi/d\gamma$  are then evaluated by Equations (B1)–(B5).

To simplify the computation, the velocity field in the mold domain is assumed to be zero, which means that the nodal coordinates in the mold domain, except the interface with the composite, do not change with the design variable. This assumption leads to some distortion of the elements in the mold domain along the interface of the mold and composite. Since the springforward angle is typically small in unidirectional composite parts, the change in the mold angle also remains small, and the mesh distortion in the mold is usually minor. It is important to note, however, that such simplification is only justified for a small change in the mold angle. Convergence studies have been performed by refining the mesh in the mold, and have shown that a slight change in the mold mesh has almost no effect on the final result.

## REFERENCES

1. Pagliuso, S. (1982). Warpage, a nightmare for composite parts producers. In: *Proceedings of the 4th International Conference on Composite Materials (ICCM-4)*. Tokyo, Japan. pp. 1617–1623.
2. Zhu, Q., Li, M., Geubelle, P.H. and Tucker III, C.L. (2000). Dimensional accuracy of thermoset composites: simulation of process-induced residual stresses. To appear in *Journal of Composite Materials*.
3. Weitsman, Y. (1980). Optimal cool-down in linear viscoelasticity. *Journal of Applied Mechanics*, **47**: 35–39.
4. White, S.R. and Hahn, H.T. (1992). Cure cycle optimization for the reduction of processing-induced residual stress in composite materials. *Journal of Composite Materials*, **27**(14): 1352–1378.
5. Olivier, P. and Cottu, J.P. (1998). Optimization of the co-curing of two different composites with the aim of minimizing residual curing stress levels. *Composites Science and Technology*, **58**: 645–651.
6. Reuter, R.C., Jr. (June 1988). Evaluation and controls of residual states in curved, composite panels. In: *Proceedings of the Fourth Japan-U.S. Conference on Composite Materials*. Washington, D.C. pp. 742–751.

7. Fernlund, G. and Poursartip, A. (1999). The effect of tooling material, cure cycle, and tool surface finish on spring-in of autoclave processed curved composite parts. In: *Proceedings of the 12th International Conference on Composite Materials (ICCM-12)*. Paris, France. p. 708. 5–9 July.
8. Li, M., Zhu, Q., Geubelle, P.H. and Tucker III, C.L. (2001). Optimal curing for thermoset matrix composites: thermochemical considerations. *Polymer Composites*, **22**(1): 118–131.
9. Morthland, T.E., Byrne, P.E., Tortorelli, D.A. and Dantzig, J.A. (August 1995). Optimal riser design for metal castings. *Metallurgical and Materials Transactions B*, **26B**: 871–885.
10. Johnston, A., Hubert, P., Nelson, K. and Poursartip, A. (1998). A sensitivity analysis of factors affecting the warpage of a composite structure. In: *Proceedings of 43rd International SAMPE Symposium and Exhibition*. CA, USA: Anaheim. May 31–June 4.
11. Fernlund, G., Poursartip, A., Nelson, K., Wilenski, M. and Swanstrom, F. (1999). Process modeling for dimensional control – sensitivity analysis of a composite spar process. In: *Proceedings of 44th International SAMPE Symposium and Exhibition*. Long Beach, California. pp. 1744–1755. 23–27 May.
12. Christensen, R.M. (1971). *Theory of Viscoelasticity*. New York: Academic Press.
13. Taylor, R.L., Pister, K.S. and Goudreau, G.L. (1970). Thermomechanical analysis of viscoelastic solids. *International Journal for Numerical Methods in Engineering*, **2**(1): 45–59.
14. Tortorelli, D.A., Tiller, M.M. and Dantzig, J.A. (1994). Optimal design of nonlinear parabolic systems. Part I: Fixed spatial domain with applications to process optimization. *Computer Methods in Applied Mechanics and Engineering*, **113**: 141–155.
15. Tortorelli, D.A., Tomasko, J.A., Morthland, T.E. and Dantzig, J.A. (1994). Optimal design of nonlinear parabolic systems. Part II: Variable spatial domain with applications to casting optimization. *Computer Methods in Applied Mechanics and Engineering*, **113**: 157–172.
16. Michaleris, P., Tortorelli, D.A. and Vidal, C.A. (1994). Tangent operators and design sensitivity formulations for transient non-linear coupled problems with applications to elastoplasticity. *International Journal for Numerical Methods in Engineering*, **37**: 2471–2499.
17. Engineering, V. (1992). *DOT Users Manual, Version 3.00*. Goleta, CA: Vanderplaats, Miura and Associates, Inc.
18. Kim, K.S. and Hahn, H.T. (1989). Residual stress development during processing of graphite/epoxy composites. *Composites Science and Technology*, **36**(2): 121–132.
19. Oakeshott, J.L. and Lemoine, D. (1998). Experimental study of spring forward in cured laminated U-channels made from unidirectionally reinforced carbon fiber-epoxy prepregs. *Plastics, Rubber and Composites Processing and Applications*, **27**(4): 190–199.
20. Radford, D.W. and Diefendorf, R.J. (1993). Shape instabilities in composites resulting from laminate anisotropy. *Journal of Reinforced Plastics and Composites*, **12**(1): 58–75.
21. Huang, C.K. and Yang, S.Y. (1997). Study on accuracy of angled advanced composite tools. *Materials and Manufacturing Process*, **12**(3): 473–486.
22. Lee, C.C. (1995). A finite element study of bond-line-read-out. *Journal of Reinforced Plastics and Composites*, **14**: 1226–1249.